Activated porous carbon nanofibers using Sn segregation for high-performance electrochemical capacitors

Geon-Hyoung An, Hyo-Jin Ahn *

Department of Materials Science and Engineering, Seoul National University of Science and Technology, Seoul 139-743, Republic of Korea

A R T I C L E   I N F O

A B S T R A C T

Activated porous carbon nanofibers (CNFs) with three different types of porous structures, which were controlled to contain 1, 4, and 8 wt% of Sn–poly(vinylpyrrolidone) (PVP) precursors in the core region and 7 wt% polyaniline (PAN)–PVP precursors in the shell region during electrospinning, were synthesized using a co-electrospinning technique with H_2-reduction. The formation mechanisms of activated porous CNF electrodes with the three different types of samples were demonstrated. The activated porous CNFs, for use as electrodes in high-performance electrochemical capacitors, have excellent capacitances (289.0 F/g at 10 mV/s), superior cycling stability, and high energy densities; these values are much better than those of the conventional CNFs. The improved capacitances of the activated porous CNFs are explained by the synergistic effect of the improved porous structures in the CNF electrodes and the formation of activated states on the CNF surfaces.

1.   Introduction

Carbon-based materials such as graphite, fullerenes, graphene, carbon nanotubes (CNTs), and carbon nanofibers (CNFs) have recently received increasing attention in both the industry and academia for use in applications such as electrical energy-storage devices (e.g., electrochemical capacitors, Li-ion batteries, and catalysts for fuel cells), photovoltaic devices (e.g., dye-sensitized solar cells and transparent conducting electrodes), and environmental applications (e.g., antimicrobial agents, sorbents, and environmental sensors) [1–3]. Among the various carbon allotropes, CNFs are attracting increasing interest because of their unique and interesting properties such as excellent electrical resistance ($\sim 10^{-7}$ to $10^{-5}\,\Omega\,m$), large surface areas (448 m^2/g), and excellent thermal and chemical stability [4–7]. Since the 1960s, various methods for CNF syntheses such as chemical vapor deposition, vapor-grown CNFs, template-directed methods, and

electrospinning, have been rapidly developed [8–11]. Among these synthetic methods, the electrospinning method, which can produce fibers with diameters of approximately 50–500 nm and lengths in the order of meters and more, is a versatile and attractive method for fabricating various nanofibers such as polymers, ceramics, carbon, and their composites [12]. Electrospinning has many advantages, including different morphological modifications, a simple process, good repeatability, and large-scale production [13,14].

Electrochemical capacitors, which store electrical energy in the electrical double-layer that forms at the interface between an electrode and an electrolyte, are generally classified according to the two different mechanisms involved. One is electrical double-layer capacitors (EDLCs), involving a non-Faradic process, which use carbon-based materials such as activated carbon, graphene, CNTs, or CNFs. The other is pseudocapacitors, involving a Faradic process, using RuO_2, MnO_2, Co_3O_4, and conducting polymers (e.g., polythiophene,

polypyrrole, and polyaniline). Despite the fact that the pseudocapacitors have relatively high energy densities because of redox reactions, disadvantages such as high cost and relatively low rate capabilities are barriers to their industrialization. In contrast, EDLCs have advantages such as good cycling stabilities, high rate capabilities, and high power densities (compared to most conventional battery systems and most pseudocapacitors) and disadvantages such as relatively low energy densities. Overcoming these disadvantages is vital for obtaining high-performance EDLCs. High surface areas, pore structures, and electrical conductivities of the electrode have been suggested to be key issues in improving electrode performance in EDLCs [15–18]. Among these factors, morphological control using the porous structures of electrodes is crucial. For examples, Chen et al. reported the synthesis of nitrogen-doped porous CNFs as efficient electrodes for supercapacitors that show good capacitive performance (202.0 F/g), good retention capability (81.7% capacitance retention at current densities ranging from 0.5 to 30 A/g), and good cycling stability up to 3000 cycles (above 97% of the initial capacitance at a current density of 1 A/g) [19]. Kim et al. synthesized porous CNF electrodes using electrospinning using polyacrylonitrile/poly(methyl methacrylate) fibers containing graphene and demonstrated good capacitance (128 F/g) of CNFs, good cycling stability up to 100 cycles (87% of the initial capacitance at a current density of 1 mA/cm^2) because of the enhanced surface area, and good electrical conductivity for high-performance supercapacitors [20]. The synthesis of activated porous CNFs using Sn segregation, which could be useful in high-performance electrochemical capacitors, has not yet been studied. Here, we synthesized activated porous CNFs using co-electrospinning with H$_2$-reduction. CNFs had enhanced specific surface areas (~1082.1 m^2/g), total pore volumes (0.64 cm^3/g), and volume percentages of meso-pores (35.0%) compared with conventional CNFs. We also successfully demonstrated their electrochemical properties such as capacitance, high rate capability, and high capacitance retention for high-performance electrochemical capacitors.

2. Experimental

2.1. Chemicals

All the reagents were purchased from Sigma–Aldrich and were analytical grade. They were used without further purification.

2.2. Synthesis of activated porous CNFs

Activated porous CNFs were synthesized using a co-electrospinning method with H$_2$-reduction method. In order to synthesize the porous CNFs, we prepared two coaxial capillaries consisting of an 18-gauge outer capillary (the shell region) and a 28-gauge inner capillary (the core region), as shown in Fig. 1a. First, the precursor solution in the shell region was prepared by dissolving 7 wt% polyacrylonitrile (PAN, $M_w = 150,000$) and 3 wt% poly(vinylpyrrolidone) (PVP, $M_w = 1,300,000$ g/mol) in N,N-dimethylformamide (DMF). In
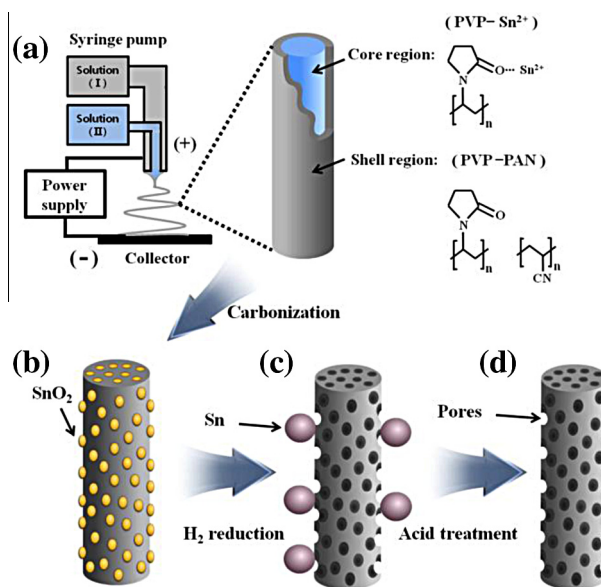

Fig. 1 – Co-electrospinning apparatus consisting of a spinneret (with two coaxial capillaries) connected to a high-voltage power supply, syringe pump, and grounded collector (a). Ideal schematic illustration for obtaining porous CNF electrodes synthesized using co-electrospinning method with H$_2$-reduction. SnO$_2$ nanophases embedded in CNFs after calcination at 800 °C under N$_2$ gas (b). Agglomerated Sn nanophases formed outside porous CNFs during H$_2$-reduction (c). Fig. 1d presents activated porous CNFs obtained after acid treatment using a mixed solution (1:1 v/v) of HF and HNO$_3$ (d).

order to systematically synthesize three different types of porous structures, the precursor solution in the core-region was controlled to contain 1, 4, and 8 wt% tin(II) chloride dihydrate (SnCl$_2$2H$_2$O) (referred to as samples A–C, respectively) with 3 wt% PVP polymer dissolved in DMF. The feeding rates of the shell region and core region solutions were fixed at 0.04 mL/h and 0.02 mL/h, respectively. For all the samples, a constant voltage of 18 kV was applied to the capillary tip, and the distance between the capillary tip and the collector was fixed at ~15 cm. The humidity in the electrospinning chamber was controlled at ~20%. The as-spun samples, which were composed of Sn metal precursor–PAN composite NFs, were heat-treated using a tube furnace at a heating rate of 5 °C/min, stabilized at 280 °C for 5 h in an air atmosphere, and then carbonized at 800 °C for 3 h in N$_2$ gas (99.999%). After calcination at 800 °C, SnO$_2$–CNF composites were formed. In order to obtain the porous CNF structure, a reduction method was performed using H$_2$ gas (N$_2$:H$_2$ = 90%:10%) at 600 °C for 15 h at 50 standard cm^3/min to transform the SnO$_2$ phases to Sn phases. The porous Sn–CNF composites were successfully obtained after the reduction. Finally, in order to obtain porous CNFs without Sn phases, an acid treatment using a mixed solution (1:1 v/v) of HF and HNO$_3$ for 5 h at room temperature to remove the Sn phases was conducted. The porous CNFs were also activated by acid treatment.

2.3. Field-emission scanning electron microscopy (FESEM) and transmission electron microscopy (TEM)

The structures and morphologies of the samples were characterized using FESEM (Hitachi S-4700) and TEM (JEOL, KBSI Suncheon Center) with selected-area electron diffraction (SAED) patterns. All the samples for FESEM measurements were prepared using ion sputtering (Hitachi E-1045); Pt ions were sputtered on the samples for 30 s. TEM images were obtained as bright-field images at an accelerating voltage of 200 kV. The samples were dispersed in ethanol for TEM measurements and placed on a carbon grid (200 mesh); the grid was allowed to dry in a vacuum oven.

2.4. Powder X-ray diffraction (XRD)

The crystalline phases, degrees of crystallinity, and structural properties of the samples were examined by XRD using a Rigaku X-ray diffractometer (D/Max 2500 V) equipped with a Cu K_α source. For XRD measurements, the samples were mounted on glass microscope slides placed on an Al holder. Data were collected with a step size of 0.02° in the range 10–80° (2 Theta) at room temperature.

2.5. Brunauer–Emmett–Teller (BET) measurements

The specific surface areas and pore structures of the CNF electrodes were measured using the BET method by N_2 adsorption at 77 K. The measurements were performed using a Micromeritics ASAP2010 accelerated surface area system; the amount of N_2 that was adsorbed as a monolayer was measured. The surface areas, total pore volumes, average pore diameters, and pore-size distributions of the CNF electrodes using BET Plot and BJH (Barrett–Joyner–Halenda) Plot were calculated from the numbers of molecules adsorbed.

2.6. Fabrication of electrode and electrolyte

The electrochemical properties of the samples were measured with potentiostat/galvanostat (PGST302 N, Eco Chemie, the Netherlands) using a conventional three-electrode system [21–28]. The working electrode, counter electrode, and reference electrode used for the three-electrode system were the as-prepared samples, Pt gauze, and Ag/AgCl (sat. KCl), respectively. To fabricate the working electrode, slurries consisting of 70 wt% as-prepared sample, 20 wt% acetylene black, and 10 wt% poly(vinylidene fluoride) binder were dissolved in N-methyl-2-pyrrolidinone. The mixture inks (3 μL) were loaded on a glassy carbon working electrode using a micropipette and then dried at 70 °C for 30 min in a vacuum oven. The mass and thickness of the electrode in a three electrode system was fixed with ~1.85 mg/cm^2 and ~50 μm. A 0.5 M H_2SO_4 solution was used as the electrolyte. The two-electrode configuration was fabricated with two symmetric electrodes using Ni foam (~90 μm thickness) as the current collector. The mass and thickness of the electrode was fixed with ~1.77 mg/cm^2 and ~100 μm. A 6 M KOH aqueous solution was used as the electrolyte for the two-electrode configuration.

2.7. Electrochemical measurements

The capacitance behaviors of the CNF electrodes were evaluated using a CV technique in the potential range 0.0–1.0 V (vs. Ag/AgCl) at scan rates of 1, 5, 10, 30, 50, and 100 mV/s, at room temperature. The cell performance of the two-electrode configuration was evaluated by galvanostatically charging and discharging the cell at a current density of 0.2–20 A/g in the potential range of 0–1 V using a WMPG 1000s battery cycler system (Won-A Tech Corp., Korea).

3. Results and discussion

Fig. 1 presents a schematic illustration of our strategy for synthesizing porous CNFs via co-electrospinning with H_2-reduction. A co-electrospinning apparatus, consisting of a spinneret (with two coaxial capillaries) connected to a high-voltage power supply, a syringe pump, and a grounded collector, shown in Fig. 1a, has been widely used for the morphology control of NFs such as hollow NFs and core–shell NFs [29–37]. In this study, as-spun NFs consisting of a polyaniline–polyvinylpyrrolidone (PAN–PVP) precursor in the shell region and a SnCl$_2$–PVP precursor in the core region were synthesized using a co-electrospinning technique. After carbonization at 800 °C, SnO$_2$ nanophases embedded within the CNFs were formed as shown in Fig. 1b. Then, the SnO$_2$ nanophases embedded in the CNFs were transformed into agglomerated Sn nanophases formed outside the porous CNFs during H$_2$-reduction (Fig. 1c). Finally, the porous CNFs were formed by dissolving the Sn nanophases by an acid treatment using a mixed solution of HF and HNO$_3$ (1:1 v/v, Fig. 1d). Activated porous CNFs with the improved porous structures, which are dependent on the amount of Sn precursor, were successfully synthesized for use in high-performance electrochemical capacitors.

To elucidate the formation mechanism of the porous CNFs, three different types of samples, which were controlled to have 1, 4, and 8 wt% SnCl$_2$–PVP precursors in the core region and 7 wt% PAN–PVP precursors in the shell region, were prepared. Fig. 2a–c show FESEM images of samples A–C obtained after carbonization at 800 °C. The diameters of samples A–C are in the ranges ~125–184 nm, ~105–184 nm, and ~108–185 nm, respectively. In samples A (Fig. 2a) and B (Fig. 2b), the CNF surfaces are smooth, but sample C (Fig. 2c) has nano-spheres of SnO$_2$ nanophases on the surfaces of CNFs because of excess Sn precursors in the CNFs. Fig. 2d–f present FESEM images obtained after H$_2$-reduction, which show agglomerated Sn nanophases in all the samples, i.e., after H$_2$-reduction, SnO$_2$ nanophases in and on the CNFs were transformed into Sn nanophases, which simultaneously emerged from the surfaces of the CNFs and agglomerated, as shown in the inset of Fig. 2f. That is, because H$_2$ gas and oxygen in SnO$_2$ nanophases tend to be encountered, the Sn nanophases are extracted out and Sn aggregates on the CNF surfaces are simultaneously formed during H$_2$-reduction at 600 °C. Therefore, porous CNFs with agglomerated Sn nanospheres were formed because of the space vacated by the SnO$_2$ nanophases. In order to synthesize conventional porous CNFs without metallic Sn agglomerates, an acid treatment
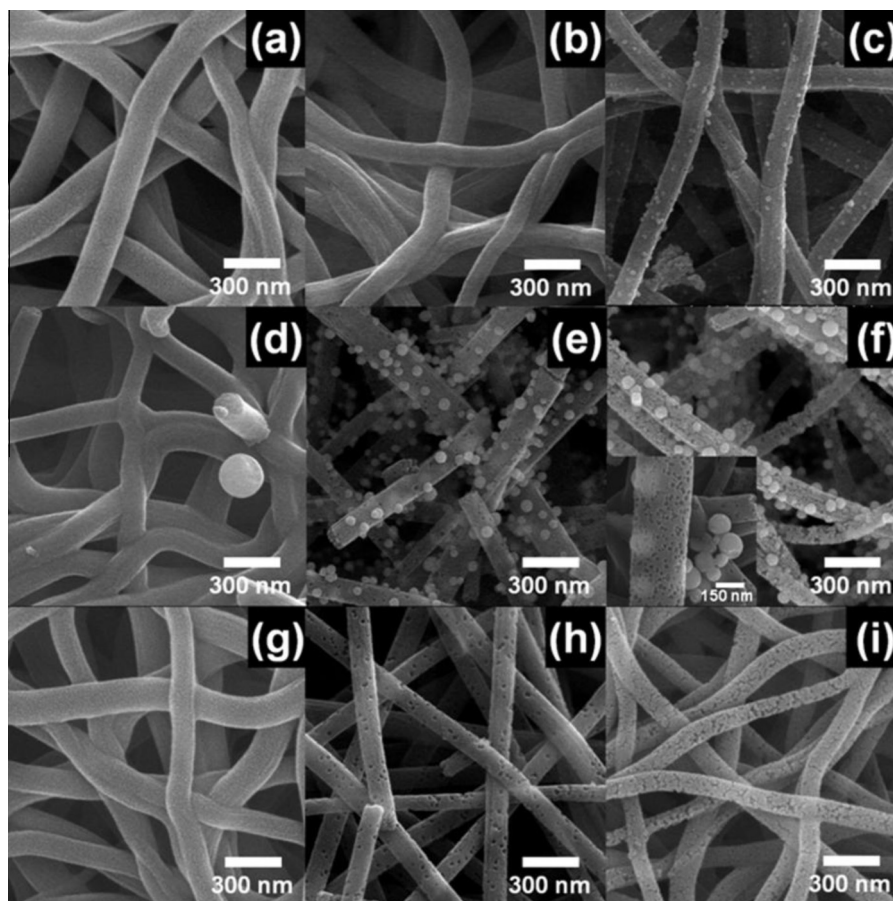
Fig. 2 – FESEM images of samples A, B, and C obtained after carbonization at 800 °C under N$_2$ gas (a–c), after H$_2$-reduction (d–f), and after acid treatment (g–i). Insert of Fig. 2f shows ongoing FESEM images of formation of agglomerated Sn nanophases on porous CNFs obtained from sample C.

using a mixed solution (1:1 v/v) of HF and HNO$_3$ was used to dissolve the Sn agglomerates. Fig. 2g–i show the FESEM images of samples A–C obtained after acid treatment. Sn agglomerates were not observed in samples A–C. Finally, the porous CNFs were successfully synthesized. The higher the loading of the Sn precursor, the more porous the CNF structure was, increased as shown in Fig. 2g–i.

To further investigate the formation mechanism of the porous CNFs, TEM measurements with selected-area electron diffraction (SAED) patterns were performed. Fig. 3a–c present TEM images of samples A–C after calcination at 800 °C. The TEM images show that SnO$_2$ nanophases, shown by dark nano-spheres, are uniformly distributed in the CNF matrix, shown by the gray contrast region. The sizes of the SnO$_2$ nanophases are in the ranges ∼3–7 nm for sample A, ∼5–31 nm for sample B, and ∼6–37 rnm for sample C. Fig. 3d–f show the TEM images of samples A–C obtained after H$_2$-reduction, which show enhanced porous structures of the CNFs with agglomerated Sn nanophases, depending on the loading amount of the Sn precursor. In particular, the inset of Fig. 3f shows a low-magnification TEM image obtained from sample C. The TEM image shows that the metallic Sn agglomerates (∼102–187 nm in size), represented by large dark nano-spheres, formed on the surfaces of the porous CNFs, while there were no Sn nanophases in the porous CNFs.

Therefore, we successfully synthesized porous CNFs with three different types of porous structures as shown in Fig. 3g–i.

To examine the porous structures of samples A–C in detail, the specific surface area, total pore volumes, average pore diameters, and pore-size distributions were determined using the BET surface area method; the results are shown in Table 1. The specific surface areas of conventional CNFs, samples A–C are ∼462.9, 633.6, 865.2, and 1082.1 m^2/g, respectively. This shows that the specific surface area of sample C is 2.3 times higher than that of the conventional CNFs. In addition, the total pore volumes and average pore diameters are 0.22 cm^3/g and 1.91 nm for conventional CNFs; 0.31 cm^3/g and 2.01 nm for sample A; 0.48 cm^3/g and 2.24 nm for sample B; and 0.64 cm^3/g and 2.39 nm for sample C. For pore-size distributions, the volume percentages of micropores (pore width <2 nm) and mesopores (pore width 2–50 nm, IUPAC classification) are, respectively, 80.1% and 19.9% for conventional CNFs; 76.4% and 23.6% for sample A; 72.5% and 27.5% for sample B; and 65.0% and 35.0% for sample C. These results imply that as the loading of the Sn precursor in the CNFs increased, the volume percentage of mesopores in the CNFs systematically increased, indicating that loading can affect the performance of electrochemical capacitors, as previously reported [38–41].
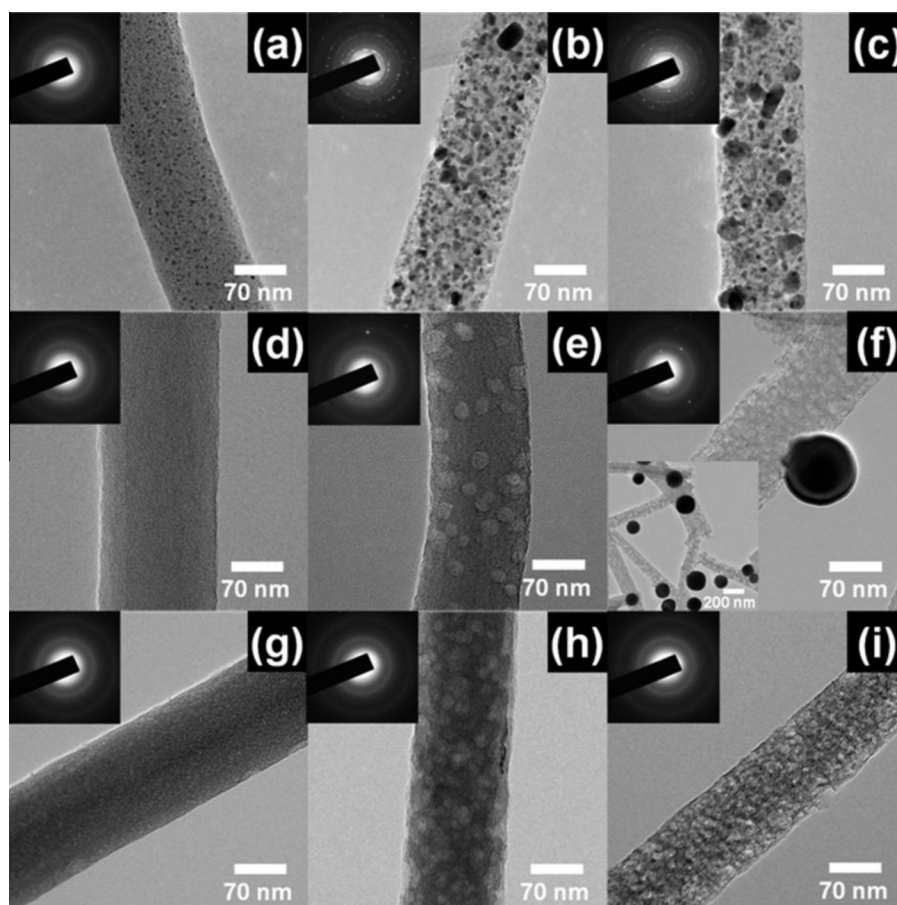
Fig. 3 – TEM images of samples A–C obtained after calcination at 800 °C under N_2 gas (a–c), after H_2-reduction (d–f), and after acid treatment (g–i). Insert of Fig. 3f shows a low-magnification TEM image obtained from sample C (Fig. f).

Table 1 – Summary of specific surface area (S_{BET}), total pore volume, average pore diameter, and pore-size distribution data for conventional CNFs, samples A–C. V_{micro} (%) and V_{meso} (%) are volume percentages of micro-pores and mesopores, respectively.

Samples	S_{BET} [$m^2 g^{-1}$]	Total pore volume ($p/p_0 = 0.990$) [$cm^2 g^{-1}$]	Average pore diameter[nm]	Pore size distribution	
				v_{micro} (%)	v_{meso} (%)
Conventional (Untreated) CNF$_s$	462	0.2213	1.91	80.1	19.9
Sample A	633	0.3164	2.01	76.4	23.6
Sample B	865	0.4861	2.24	72.5	27.5
Sample C	1082	0.6487	2.39	65.0	35.0

In particular, the pore size distribution and pore volumes in the active materials are very important characteristics for high-performance electrochemical capacitors. Fig. 4 shows the pore size distributions and the pore volumes obtained from the N_2 adsorption isotherms using BJH method, in which the pore sizes range from 2.4 to 10 nm. Sample C exhibits the highest mesopore volume, with peak pore sizes ranging from 2.4 to 4.2 nm because of the increased loading of the Sn precursor in the CNFs. The enhanced mesopores of sample C can provide low resistance pathways and a shorter diffusion route for ions because of the admission of larger amounts of electrolytes into the pore volumes. Therefore, the enhanced mesopores advance ionic transport in EDLCs, which

results in high performance of the electrochemical capacitors [42]. Thus, improvements in the porous structures, such as enhanced specific surface areas, total pore volumes, and volume percentages of mesopores, directly affect the performances of electrochemical capacitors.

Fig. 5a–c present powder XRD data obtained after calcination in N_2 gas, H_2 reduction, and acid treatment to investigate the structures and crystallinities of samples A–C. The XRD results (Fig. 5a) indicate that the main characteristic diffraction peaks of samples A–C obtained after calcination at 800 °C under N_2 gas were observed at 26.5°, 33.9°, 37.9°, and 51.7°, corresponding to the (110), (101), (200), and (211) planes. The XRD patterns of samples A–C are in good
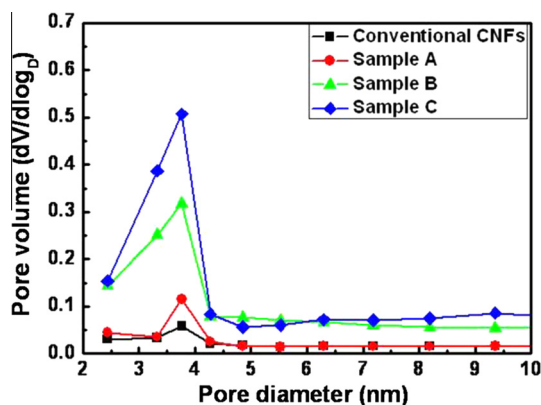
Fig. 4 – The BJH pore size distributions of the conventional CNFs, samples A–C.

agreement with those of the cassiterite SnO_2 phase, which has a tetragonal rutile structure (space group $P4_2/mnm$ [136]; JCPDS card No. 71-0652). The formation of SnO_2 phases is caused by oxygen in the PVP [$(C_6H_9NO)_n$]. In particular, in the case of sample C, characteristic diffraction peaks besides the diffraction peaks of the SnO_2 phases were observed at 30.6°, 32.0°, 43.9°, and 44.9°, corresponding to the (200), (101), (220), and (211) planes of the metallic Sn phase (body-centered tetragonal structure, I4$_1$/amd [141]). This result is explained by the increasing amount of Sn

precursors, i.e., after completion of the reaction of oxygen sources in the PVP and Sn precursors, the remaining Sn precursors are present as the metallic Sn phases after calcination at 800 °C under N_2 gas. In addition, as shown in Fig. 5b, the main characteristic diffraction peaks of samples A–C obtained after H_2 reduction were observed at 30.6°, 32.0°, 43.9°, and 44.9°, corresponding to the (200), (101), (220), and (211) planes of the body-centered tetragonal structure of the polycrystalline Sn phase (space group I4$_1$/amd [141]; JCPDS card No. 86–2264). Fig. 5c shows powder XRD data for samples A–C obtained after acid treatment. There are broad diffraction peaks at 24°, which imply amorphous CNFs. In particular, no characteristic diffraction peaks from metallic Sn nanophases are observed. Based on the FESEM, TEM, BET, and XRD results, activated porous CNFs with three different types of porous structures were successfully synthesized using co-electrospinning with H_2-reduction.

Fig. 6a–d show cyclic voltammograms (CVs) for the electro-oxidation and electroreduction properties of conventional CNFs, samples A–C, which were evaluated at scan rates of 1, 5, 10, 30, 50, and 100 mV/s in the range 0.0–1.0 V (vs. Ag/AgCl). The CVs of all the samples exhibit EDLC behavior, considering the charging–discharging current in both directions of the voltage scanning. The capacitances (C) of the samples were calculated using the following equation [43–48]:
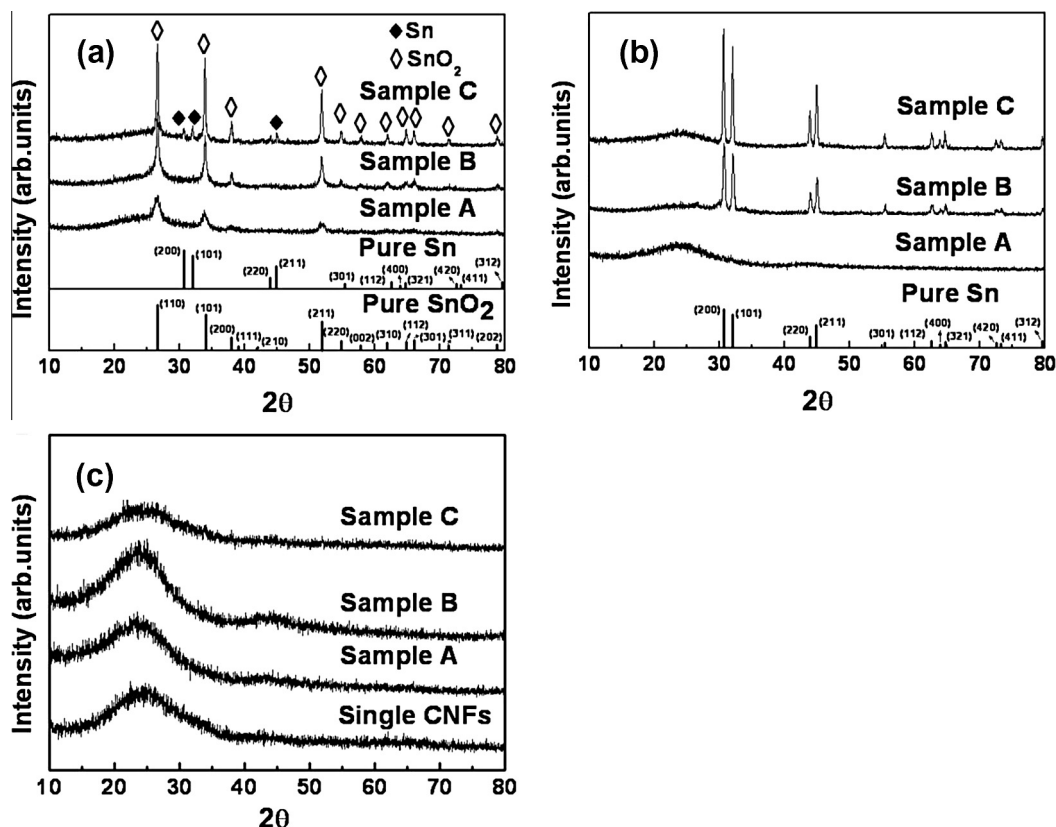
$$C = (Q_a + Q_b)/(2m\Delta V)$$

Fig. 5 – XRD patterns obtained after calcination in N_2 gas (a), H_2 reduction (b), and acid treatment using a mixed solution (1:1 v/v) of HF and HNO_3 (c) to investigate the structures and crystallinities of samples A–C, respectively. Reference bulk reflections of pure Sn and SnO_2 phases are shown at the bottom (JCPDS cards No. 04-0673 and 41-1445).
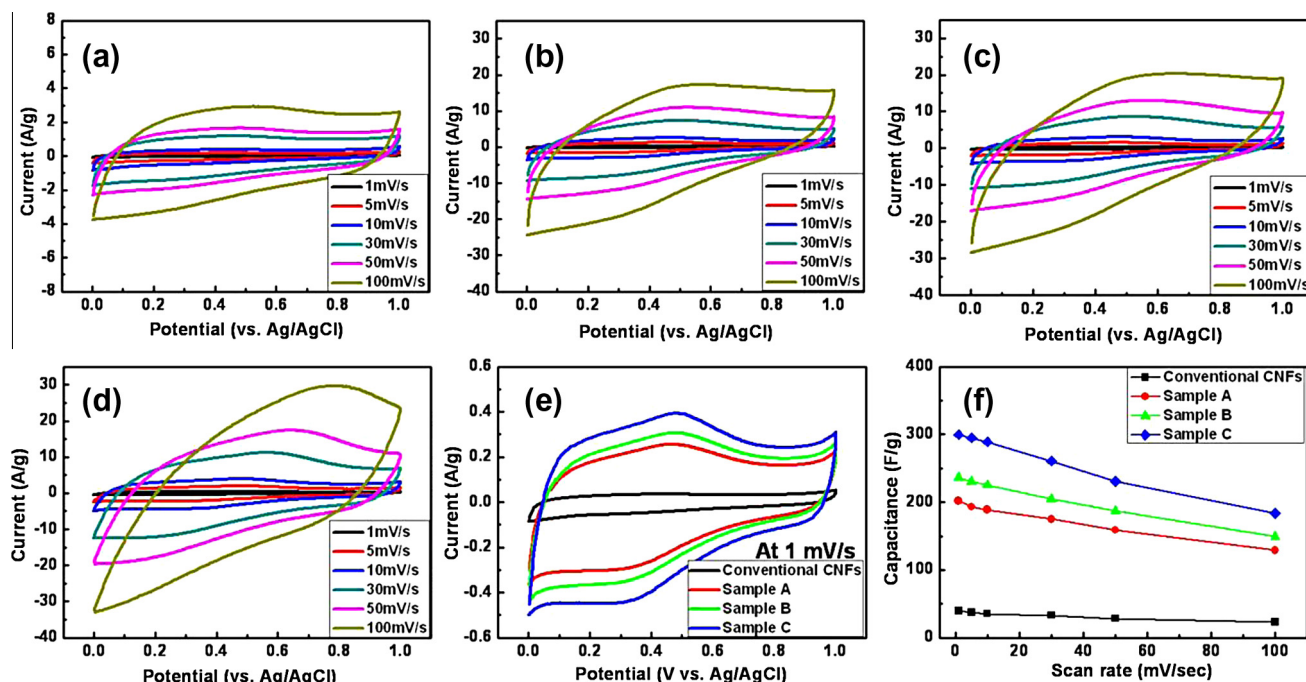
Fig. 6 – Cyclic voltammograms for electrooxidation and electroreduction properties of conventional CNFs (a), sample A (b), sample B (c), and sample C (d), evaluated using conventional three-electrode systems at potential-scan rates of 1, 5, 10, 30, 50, and 100 mV/s in the range 0.0–1.0 V (vs. Ag/AgCl). Cyclic voltammograms (e) of all the samples measured at a potential-scan rate of 1 mV/s. A function of the potential-scan rates (f) for examining the high-rate capabilities of the samples in the range 10–100 mV/s is estimated from Fig. 5(a–d).

where Q_a and Q_b are the charges of the anodic and cathodic regions, m is the mass, and ΔV is the potential range of the CVs. The conventional CNFs, samples A–C have capacitances of ~35.2, ~188.7, ~225.2, and ~289.0 F/g at 10 mV/s, i.e., the capacitance of sample C is 8.2 times higher than that of the conventional CNF electrodes used in electrochemical capacitors. The enhanced capacitance can be explained in terms of two important factors: one is the improvement in the porous structures of the CNF electrodes, such as enhanced specific surface areas, total pore volumes, and volume percentages of mesopores. As previously mentioned, the specific surface area, total pore volume, and volume percentage of mesopores in sample C are 2.3, 2.9, and 1.7 times higher, respectively, compared with those of conventional CNFs. The other factor is the transformation of the original states to activated states on the CNF surfaces, which occurs during acid treatment. For activated CNFs, some researchers have reported improved electrochemical capacitances as a result of formation of functional groups such as –COOH, –OH, and >C=O on the edge surfaces of CNFs [49–54]. Therefore, activated porous CNF electrodes for electrochemical capacitors could lead to improved capacitances because of the synergistic effects of the improved porous structures in the CNFs (because of the enhanced specific surface areas, total pore volumes, and volume percentages of mesopores) and the formation of activated states on the CNF surfaces. Fig. 6e shows cyclic voltammograms of all the samples measured at a potential-scan rate of 1 mV/s in the range 0.0–1.0 V (vs. Ag/AgCl). The cyclic voltammograms reveal redox peaks at 0.4–0.5 V, which indicates pseudocapacitance behavior relative to

faradic redox reactions due to oxygen functional groups formed on the edge surfaces of activated CNFs [55]. Therefore, the improved capacitance of activated porous CNFs can be explained by a synergy effect of pseudo-capacitance and electric double-layer capacitance. The high rate capabilities of the samples were investigated, and Fig. 6f shows the capacitances characterized as a function of potential-scan rate, estimated from Fig. 6a–d. As shown in Fig. 6f, the capacitances of the conventional CNFs, samples A–C are ~22.9, ~128.8, ~148.8, and ~183.5 F/g at a scan rate of 100 mV/s, i.e., after measurements at a potential-scan rate of 100 mV/s, the capacitances of the conventional CNFs, samples A–C drop by 35%, 32%, 34%, and 36% of their initial values, respectively. In addition, the capacitances of all the samples decrease with increasing potential-scan rate. The reason for the decrease in the capacitance is the reduced diffusion time, since the ions in the electrolyte cannot fully access the surfaces of the CNFs at high potential-scan rates. In spite of the slight decreases in the capacitance when the scan rates increase up to 100 mV/s, the porous CNFs of sample C yield excellent capacitance at high potential-scan rates.

To further investigate the electrochemical performance of all the samples, galvanostatic charge/discharge measurements were performed using the symmetric two-electrode configuration at 0.5 A/g in the range 0.0–1.0 V, as shown in Fig. 7a. The discharge times of the samples are observed to be 20 s for conventional CNFs, 101 s for sample A, 128 s for sample B, and 167 s for sample C. It is noted that sample C exhibits the best capacitance behavior at a constant current density of 0.5 A/g. In addition, the triangular charge/discharge
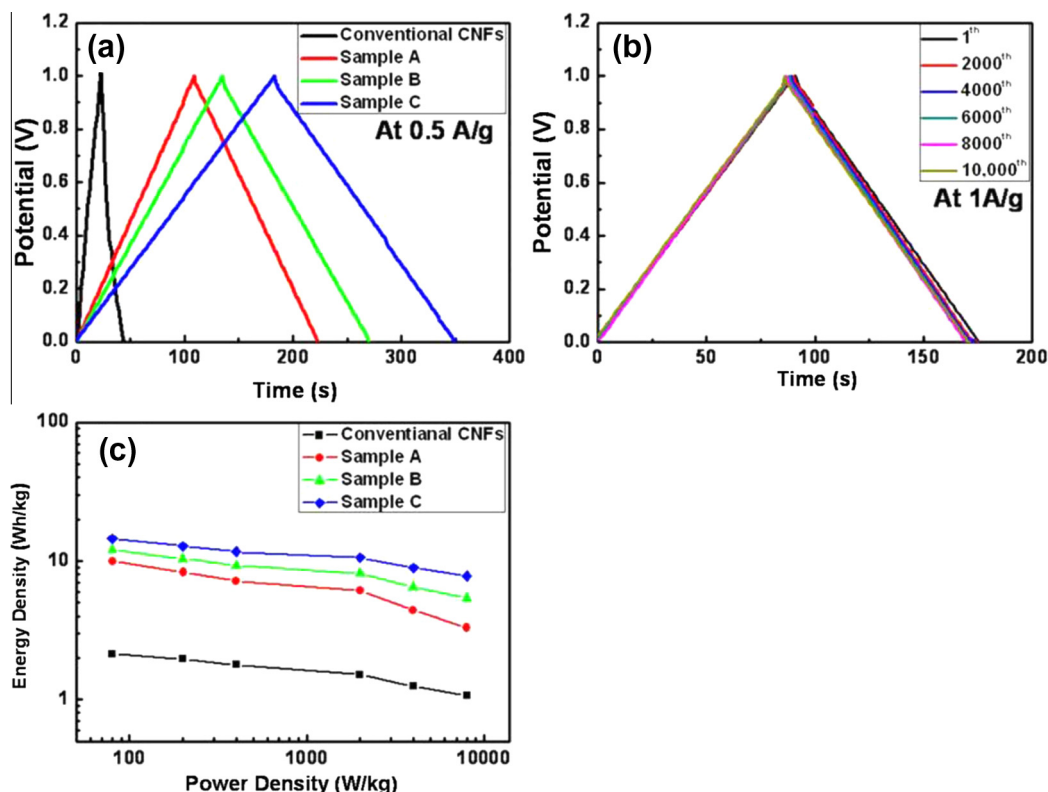
Fig. 7 – Galvanostatic charge/discharge curves evaluated using symmetric two-electrode cells in 6 M KOH at 0.5 A/g (a). Charge/discharge curves after each 2000 cycles for sample C at a current density of 1.0 A/g (b). A Ragone plot for conventional CNFs, samples A–C calculated by varying the discharging current density of 0.2, 0.5, 1, 5, 10, and 20 A/g (c).

curves have linear slopes and excellent bilateral symmetry for the porous capacitors, implying ideal capacitance. Fig. 7b shows the cycling stability of sample C in the two-electrode configuration, for which results were obtained after the 1st, 2000th, 4000th, 6000th, 8000th, and 10,000th cycles at a current density of 1 A/g. The charge/discharge curves in Fig. 7b were almost unchanged up to 10,000 cycles. Therefore, the activated porous CNF electrodes have excellent cycling stability up to 10,000 cycles [56]. In order to determine the energy density (E, Wh /kg) and power density (P, W/kg), a Ragone plot was calculated using the following equations [57–59]:

$$E = 0.5 \cdot C \cdot (\Delta V)^2 / 3.6$$

$$P = E \cdot 3.6 / \Delta t$$

where C is the device capacitance measured using two-electrode cells, ΔV represents the discharge curves excluding initial drop (V), and Δt is the discharge time (s). As shown in the Fig. 7c, the Ragone plots were obtained by varying the discharging current density to 0.2, 0.5, 1, 5, 10, and 20 A/g while varying the power density over the range of 80–8000 W/kg. Sample C exhibits the highest energy density (~14.4–7.7 W h/kg) among the capacitors and achieves a higher value than those of currently reported carbon-based electrochemical capacitors [19,60,61]. Thus, their capacitances, cycling stabilities, and energy densities show that activated porous CNFs are promising candidates for use as electrodes in high-performance electrochemical capacitors.

4. Conclusions

Activated porous CNF electrodes were successfully synthesized using a co-electrospinning technique with H_2-reduction method. To systematically investigate the porous structures of CNFs, Sn precursors with a PVP polymer, dissolved in N,N-dimethylformamide (DMF), were infiltrated at levels of 1 wt% (sample A), 4 wt% (sample B), and 8 wt% (sample C) into the electrospinning core region. Sample C exhibited an improved specific surface area (1082.1 m^2/g), total pore volume (0.64 cm^3/g), and volume percentage of mesopores (35.0%). For electrochemical capacitors, sample C showed superior electrochemical properties such as high capacitance (289.0 F/g at 10 mV/s), superior cycling stability, and high energy densities compared to those of conventional CNFs, sample A, and sample B. The enhanced performances of the activated porous CNF electrodes are attributed to the combined effects of the improved porous structures of CNF electrodes and formation of activated states on the CNF surfaces. Therefore, the introduction of activated porous CNFs could be a key technology for fabricating high-performance electrochemical capacitors.

Acknowledgments

REFERENCES

[1] Inagaki M, Yang Y, Kang F. Carbon nanofibers prepared via electrospinning. Adv Mater 2012;24:2547–66.

[2] Lee JS, Kwon OS, Park SJ, Park EY, You SA, Yoon H, et al. Fabrication of ultrafine metal-oxide-decorated carbon nanofibers for DMMP sensor application. ACS Nano 2011;5(10):7992–8001.

[3] Mauter MS, Elimelech M. Environmental applications of carbon-based nanomaterials. Environ Sci Technol 2008;42(16):5843–59.

[4] Pan D, Ombaba M, Zhou Z-Y, Liu Y, Chen S, Lu J. Direct growth of carbon nanofibers to generate a 3D porous platform on a metal contact to enable an oxygen reduction reaction. ACS Nano 2012;6(12):10720–6.

[5] Spender J, Demers AL, Xie X, Cline AE, Earle MA, Ellis LD, et al. Method for production of polymer and carbon nanofibers from water-soluble polymers. Nano Lett 2012;12:3857–60.

[6] Lee MK, Dillen AJ, Bitter JH, Jong KP. Deposition precipitation for the preparation of carbon nanofiber supported nickel catalysts. J Am Chem Soc 2005;127:13573–82.

[7] Bezemer GL, Bitter JH, Kuipers HPCE, Oosterbeek H, Holewijn JE, Xu X, et al. Cobalt particle size effects in the Fischer-Tropsch reaction studied with carbon nanofiber supported catalysts. J Am Chem Soc 2006;128:3956–64.

[8] Fan Z-J, Yan J, Wei T, Ning G-Q, Zhi L-J, Liu J-C, et al. Nanographene-constructed carbon nanofibers grown on graphene sheets by chemical vapor deposition: high-performance anode materials for lithium ion batteries. ACS Nano 2011;5(4):2787–94.

[9] Al-Saleh MH, Sundararaj U. A review of vapor grown carbon nanofiber/polymer conductive composites. Carbon 2009;47(1):2–22.

[10] Zheng G, Yang Y, Cha JJ, Hong SS, Cui Y. Hollow carbon nanofiber-encapsulated sulfur cathodes for high specific capacity rechargeable lithium batteries. Nano Lett 2011;11:4462–7.

[11] Kim C, Ngoc BTN, Yang KS, Kojima M, Kim YA, Kim YJ, et al. Self-sustained thinwebs consisting of porous carbon nanofibers for supercapacitors via the electrospinning of polyacrylonitrile solutions containing zinc chloride. Adv Mater 2007;19:2341–6.

[12] Rmakrishna S, Fujihara K, Teo WE, Lim TC, Ma Z. An introduction to electrospinning and nanofibers. World Scientific Publishing Co Ltd.; 2005.

[13] An HL, Ahn H-J. Fabrication of wrinkled Nb-doped TiO_2 nanofibres via electrospinning. Mater Lett 2013;93:88–91.

[14] Zheng J, Liu K, Reneker DH, Becker ML. Post-assembly derivatization of electrospun nanofibers via strain-promoted azide alkyne cycloaddition. J Am Chem Soc 2012;134:17274–7.

[15] Itoi H, Nishihara H, Kogure T, Kyotani T. Three-dimensionally arrayed and mutually connected 1.2-nm nanopores for high-performance electric double layer capacitor. J Am Chem Soc 2011;133:1165–7.

[16] Lai L, Yang H, Wang L, Teh BK, Zhong J, Chou H, et al. Preparation of supercapacitor electrodes through selection of graphene surface functionalities. ACS Nano 2012;6(7):5941–51.

[17] Korenblit Y, Rose M, Kockrick E, Borchardt L, Kvit A, Kaskel S, et al. High-rate electrochemical capacitors based on ordered mesoporous silicon carbide-derived carbon. ACS Nano 2010;4(3):1337–44.

[18] Sharama P, Bhatti TS. A review on electrochemical double-layer capacitors. Energ Convers Manag 2010;51:2901–12.

[19] Chen L-F, Zhang X-D, Liang H-W, Kong M, Guan Q-F, Chen P, et al. Synthesis of nitrogen-doped porous carbon nanofibers as an efficient electrode material for supercapacitors. ACS Nano 2012;6(8):7092–102.

[20] Kim B-H, Yang KS, Ferraris JP. Highly conductive, mesoporous carbon nanofiber web as electrode material for high-performance supercapacitors. Electrochem Acta 2012;75:325–31.

[21] An G-H, Ahn H-J. Carbon nanofibre composites decorated with Ru-Ag nanophases for high-efficiency electrochemical capacitors. Electrochm Solid-State Lett 2013;2(5):M33–6.

[22] Hu C-C, Guo H-Y, Chang K-H, Huang C-C. Anodic composite deposition of $RuO_2 \cdot xH_2O$-TiO$_2$ for electrochemical supercapacitors. Electrochem Commun 2009;11:1631–4.

[23] Zhang W, Huang Z-H, Cao G, Kang F, Yang Y. A novel mesoporous carbon with straight tunnel-like pore structure for high rate electrochemical capacitors. J Power Sources 2012;204:230–5.

[24] Lee J-B, Jeong S-Y, Moon W-J, Seong T-Y, Ahn H-J. Preparation and characterization of electro-spun RuO_2-Ag$_2$O composite nanowires for electrochemical capacitors. J Alloys Compd 2011;509:4336–40.

[25] Rios EC, Rosario AV, Mello RMQ, Micaroni L. Poly(3-methylthiophene)/MnO$_2$ composite electrodes as electrochemical capacitors. J Power Sources 2007;163:1137–42.

[26] Reddy RN, Reddy RG. Synthesis and electrochemical characterization of amorphous MnO$_2$ electrochemical capacitor electrode material. J Power Sources 2004;132:315–20.

[27] Adelkhani H, Didehban K, Hayasi M. Performance evaluation of polyacrylamide/silver composite as electrode material in electrochemical capacitor. Curr Appl Phys 2013;13:522–5.

[28] Duay J, Sherrill SA, Gui Z, Gillette E, Lee SB. Self-limiting electrodeposition of hierarchical MnO$_2$ and M(OH)$_2$/MnO$_2$ nanofibril/nanowires: mechanism and supercapacitor properties. ACS Nano 2013;7(2):1200–14.

[29] Zhang Y, Huang Z-M, Xu X, Lim CT, Ramakrishna S. Preparation of core-shell structured PCL-r-Gelatin Bi-component nanofibers by coaxial electrospinning. Chem Mater 2004;16:3406–9.

[30] Chen H, Wang N, Di J, Zhao Y, SongY Y, Jiang L. Nanowire-in-microtube structured core/shell fibers via multifluidic coaxial electrospinning. Langmuir 2010;26(13):11291–6.

[31] Sun Z, Zussman E, Yarin AL, Wendorff JH. A Greiner. Compound core-chell polymer nanofibers by co-electrospinning. Adv Mater 2003;15(22):1929–32.

[32] An G-H, Ahn H-J. Fabrication of PtRu/Ru coreeshell nanowires by exchanging Ru phases. Solid State Sci 2012;14:1050–4.

[33] Li D, Xia Y. Direct fabrication of composite and ceramic hollow nanofibers by electrospinning. Nano Lett 2004;4(5):933–8.

[34] An G-H, Ahn H-J. Fabrication of SnO$_2$ and SiO$_2$ nanoparticle-embedded carbon nanofiber composites via co-electrospinning. Ceram Int 2012;38:3197–201.

[35] Wang C, Yan K-W, Lin Y-D, Hsieh PCH. Biodegradable core/shell fibers by coaxial electrospinning: processing, fiber characterization, and its application in sustained drug release. Macromolecules 2010;43:6389–97.

[36] McCann JT, Marquez M, Xia Y. Melt coaxial electrospinning: a versatile method for the encapsulation of solid materials and fabrication of phase change nanofibers. Nano Lett 2006;6(12):2868–72.

[37] Muthiah P, Hsu S-H, Sigmund W. Coaxially electrospun PVDF-Teflon AF and Teflon AF-PVDF core-sheath nanofiber mats with superhydrophobic properties. Langmuir 2010;26(15):12483–7.

[38] Largeot C, Portet C, Chmiola J, Taberna P-L, Gogotsi Y, Simon P. Relation between the ion size and pore size for an electric double-layer capacitor. J Am Chem Soc 2008;130:2730–1.

[39] Kim Y-J, Lee B-J, Suezaki H, Chino T, Abe Y, Yanagiura T, et al. Preparation and characterization of bamboo-based activated carbons as electrode materials for electric double layer capacitors. Carbon 2006;44:1581–616.

[40] Thomberg T, Jänes A, Lust E. Energy and power performance of electrochemical double-layer capacitors based on molybdenum carbide derived carbon. Electrochim Acta 2010;55:3138–43.

[41] Jung M-J, Jeong EJ, Cho S, Yeo SY, Lee Y-S. Effects of surface chemical properties of activated carbon modified by amino-fluorination for electric double-layer capacitor. J Colloid Interface Sci 2012;381:152–7.

[42] Kim B-H, Kim CH, Yang KS, Rahy A, Yang DJ. Electrospun vanadium pentoxide/carbon nanofiber composites for supercapacitor electrodes. Electrochem Acta 2012;83:335–40.

[43] Kim JH, Nam K-W, Ma SB, Kim KB. Fabrication and electrochemical properties of carbon nanotube film electrodes. Carbon 2006;44:1963–8.

[44] Ahn H-J, Sung Y-E, Kim WB, Seong T-Y. Crystalline Ag nanocluster-incorporated RuO_2 as an electrode material for thin-film micropseudocapacitors. Electrochm Solid-State Lett 2008;11(7):A112–5.

[45] Nasibi M, Golozar MA, Rashed G. Nano iron oxide(Fe_2O_3)/carbonblack electrodes for electrochemical capacitors. Mater Lett 2012;85:40–3.

[46] Kim I-H, Kim J-H, Kim K-B. Electrochemical characterization of electrochemically prepared ruthenium oxide/carbon nanotube electrode for supercapacitor application. Solid-State Lett 2005;8(7):A369–72.

[47] Jayalakshmi M, Rao MM, Kim K-B. Effect of particle size on the electrochemical capacitance of α-$Ni(OH)_2$ in alkali solutions. Int J Electrochem Sci 2006;1:324–33.

[48] Nasibi M, Golozar MA, Rashed G. Nano zirconium oxide/carbon black as a new electrode material for electrochemical double layer capacitors. J Power Sources 2012;206:108–10.

[49] Maiyalagan T. Silicotungstic acid stabilized Pt-Ru nanoparticles supported on carbon nanofibers electrodes for methanol oxidation. Int J Hydrogen Energy 2009;34:2874–9.

[50] Boehm HP. Some aspects of the surface chemistry of carbon blacks and other carbons. Carbon 1994;32(5):759–69.

[51] Ros TG, Dillen AJ, Geus W, Koningsberger DC. Surface oxidation of carbon nanofibres. Chem Eur J 2002;8(5):1151–62.

[52] Shaffer MSP, Fan X, Windele AH. Dispersion and packing of carbon nanotubes. Carbon 1998;36(11):1603–12.

[53] Chen J, Hamon MA, Hu H, Chen Y, Rao AM, Eklund PC, et al. Solution properties of single-walled carbon nanotubes. Science 1998;282:95–8.

[54] Figueiredo JL, Pereira MFR, Freitas MMA, Orfao JJM. Modification of the surface chemistry of activated carbons. Carbon 1999;37:1379–89.

[55] Li Q, Jiang R, Dou Y, Wu Z, Huang T, Feng D, et al. Synthesis of mesoporous carbon spheres with a hierarchical pore structure for the electrochemical double-layer capacitor. Carbon 2011;49:1248–57.

[56] Yang L, Cheng S, Ding Y, Zhu X, Wnag ZL, Liu M. Hierarchical network architechtures of carbon fiber paper supported cobalt oxide nanonet for high-capacity pseudocapacitors. Nano Lett 2012;12:321–5.

[57] Zhang J, Zhao XS. On the configuration of supercapacitors for maximizing electrochemical performance. ChemSusChem 2012;5(5):818–41.

[58] Zheng JP, Jow TR. High energy and high power density electrochemical capacitors. J Power Sources 1996;62:155–9.

[59] Kim K, Choi M, Ryoo R. Ethanol-based synthesis of hierarchically porous carbon using nanocrystalline beta zeolite template for high-rate electrical double layer capacitor. Carbon 2013;60:175–85.

[60] Tran C, Kalra V. Fabrication of porous carbon nanofibers with adjustable pore sizes as electrodes for supercapacitors. J Power Sources 2013;235:289–96.

[61] Chen Y, Wang B, Dong S, Wang Y, Liu Y. Rectangular microscale carbon tubes with protuberant wall for high-rate electrochemical capacitors. Electrochim Acta 2012;80:34–40.